RMetS
Royal Meteorological Society

Properties of a simulated convective boundary layer over inhomogeneous vegetation

Chan Wang,[a] Wenshou Tian,[a]*Douglas J. Parker,[b] John H. Marsham[c] and Zhenhai Guo[d]
[a]*Key Laboratory for Semi-Arid Climate Change of the Ministry of Education, College of Atmospheric Sciences, Lanzhou University, Lanzhou, China*
[b]*School of Earth and Environment, University of Leeds, UK*
[c]*National Centre for Atmospheric Science, School of Earth and Environment, University of Leeds, UK*
[d]*Institute of Atmospheric Physics, CAS, China*
*Correspondence to: Wenshou Tian, College of Atmospheric Sciences, Lanzhou University, Lanzhou 730000, China.
E-mail: wstian@lzu.edu.cn

Using a high-resolution boundary-layer model, effects of heterogeneity over a mesoscale flat domain are investigated through a series of idealised model simulations. In these simulations two different land surface types (bare soil and vegetation) are arranged in two different patterns. It is found that the effect of heterogeneity remains significant with geostrophic winds of 10 m s^{-1}. However, when the geostrophic wind direction is perpendicular to the alignment of the surface heterogeneities (with alignment here defined as the direction along the edges of a sequence of surface patches), higher winds tend to weaken the coherent circulations caused by the surface heterogeneities. The vertical winds generated by the mesoscale circulations associated with the surface heterogeneities are on the order of 0.5 cm s^{-1}. When the geostrophic wind direction is perpendicular to the alignment of the surface heterogeneities over a three-strip surface type, the mesoscale pattern in horizontal velocity is also pronounced, with significant fluctuations at the interfaces between two different surface patches. The heights at which the heterogeneity effects on potential temperature and winds vanish are well above the convective boundary layer top and reach at least 3.3 Z_i under light winds, but depend on the wind speed and directions as well as the orientation of surface heterogeneities.

Finally, the implications of the surface heterogeneity for initiation of deep convection have been explored for a surface consisting of two-dimensional strips of alternating soil and vegetated surfaces aligned in the north–south direction. For this surface pattern, the interaction between westerly background winds and the secondary circulation sets up conditions which favour the initiation of deep convection at the eastern, downwind edge of the soil strip. Copyright © 2010 Royal Meteorological Society

Key Words: convective boundary layer; surface inhomogeneities; thermal convection; heterogeneity effect

Received 6 October 2009; Revised 20 September 2010; Accepted 5 October 2010; Published online in Wiley Online Library 24 November 2010

Citation: Wang C, Tian W, Parker DJ, Marsham JH, Guo Z. 2011. Properties of a simulated convective boundary layer over inhomogeneous vegetation. *Q. J. R. Meteorol. Soc.* **137**: 99–117. DOI:10.1002/qj.724

1. Introduction

The effects of land surface inhomogeneities on the convective boundary layer (CBL) have been studied extensively in the last few decades. These studies have demonstrated that the effects of surface heterogeneities on the properties of the CBL depend on various factors including the geostrophic wind, and the scales, shapes and forms of the surface inhomogeneities, for example variations in albedo, vegetation, terrain, soil moisture and urban areas (Walko

et al., 1992; Mahrt *et al.*, 1994; Shen and Leclerc, 1995; Avissar and Schmidt, 1998; Mahrt, 2000; Albertson *et al.*, 2001; Raasch and Harbusch, 2001; Yates *et al.*, 2001; Letzel and Raasch, 2003; Patton *et al.*, 2005; Taylor *et al.*, 2007; Marsham *et al.*, 2008; Garcia-Carreras *et al.*, 2010). Avissar and Schmidt (1998) found that a weak geostrophic wind of 2.5 m s^{-1} is enough to reduce the effect of land surface inhomogeneities on the CBL while a 5 m s^{-1} geostrophic wind could eliminate all impacts of surface inhomogeneities. However, Raasch and Harbusch (2001) pointed out that the surface effect of heterogeneity on the CBL is still significant for a geostrophic wind of 7.5 m s^{-1}. Some other studies showed that relatively high background wind does not necessarily inhibit the mesoscale circulations, but usually advects them away, and that coherent advection of the mesoscale rolls by this wind is an important effect (Weaver and Avissar, 2001; Baidya Roy and Avissar, 2002; Weaver, 2004). The possible reason for this disagreement may arise from the different heterogeneity alignments with respect to wind directions used in those studies. Prabha *et al.* (2007) showed that the heat flux heterogeneity and its alignment with respect to geostrophic wind affected the strength and orientation of organized thermals, and similar results were obtained by Kim *et al.* (2004).

Land surface heterogeneities with different spatial scales also have different effects on the CBL; land surface heterogeneities at scales of tens of kilometres can induce mesoscale circulations (Gopalakrishnan *et al.*, 2000; Baidya Roy *et al.*, 2003; Kustas and Albertson, 2003; Kang *et al.*, 2007; Taylor *et al.*, 2007; Garcia-Carreras *et al.*, 2010) while heterogeneities with scales (λ) on the order of the boundary-layer height (Z_i) mainly influence various CBL properties depending on values of λ/Z_i (Prabha *et al.*, 2007; and the references therein). Baidya Roy and Avissar (2000) showed that meso-γ-scale ($2 \sim 20$ km) surface heterogeneity produces organized circulations with the same horizontal length-scale as that of the heterogeneity. However, if the length-scale of the surface heterogeneity exceeds $5 \sim 10$ km, random turbulent thermals also develop and affect their structure.

Many of the above-mentioned studies used large-eddy models (LEMs) to simulate the effect of heterogeneity on the CBL. The scales of heterogeneities in those models are generally a few kilometres due to the relatively small model domains that are possible with the high model resolutions used in LEMs. Some studies investigated the effect of heterogeneity of orography on the CBL over mesoscale model domains (e.g. Gopalakrishnan and Avissar, 2000; Tian and Parker, 2003), but the effect of heterogeneity due to other variations in the land surface was not considered. The effect of mesoscale heterogeneities on the CBL has mainly been investigated by means of case-studies (André *et al.*, 1990; Kustas and Albertson, 2003; Taylor *et al.*, 2007; Garcia-Carreras *et al.*, 2010) and there are not, thus far, many idealised systematic modelling studies. In this study we use a high-resolution boundary-layer model to re-examine the effects of mesoscale heterogeneities due to different distributions of vegetation and soil surfaces on the CBL through a series of idealised model simulations.

The differences in effects of heterogeneity between various experimental and modelling studies may arise from different scales of surface inhomogeneities under different geostrophic wind conditions (Shen and Leclerc, 1995). The major objective of this study is to investigate effects of mesoscale heterogeneity due to different patterns, i.e. different land surface vegetation distributions on convective properties under different geostrophic wind conditions. Note that many previous studies have examined the effects of mesoscale heterogeneities due to different distributions of vegetation and soil surfaces on the CBL, under different wind conditions. However, most of these studies are based on numerical simulations which are not considering such an idealised large-eddy simulation (LES)-type framework as employed in this study. Some of those studies used mesoscale models with relatively coarse resolutions to simulate heterogeneity effects over realistic mesoscale domains (e.g. Weaver and Avissar, 2001; Baidya Roy and Avissar, 2002; Baidya Roy *et al.*, 2003), while some other studies used a state-of-the-art LES and systematically analysed the effects of heterogeneity produced by idealised sensible heat flux waves and topographical features over relatively small domains (Avissar and Schmidt, 1998; Baidya Roy and Avissar, 2000; Gopalakrishnan *et al.*, 2000).

Section 2 briefly describes our model set-up and numerical experiments. The model results are discussed in section 3, including the effect of heterogeneity on bulk convective properties and local flows within the CBL. The summary and conclusions are given in section 4.

2. Model set-up and numerical experiments

The model used is the UK Met Office boundary-layer model named BLASIUS (Mason, 1987; Tian and Parker, 2002; Vosper and Brown, 2008). In order to study land–atmosphere coupling effects, a simple land surface scheme described in Tian (2002) is incorporated in the model in which the surface available energy, A, i.e. the surface net radiation, is partitioned into three parts: sensible heat flux, H_0, latent heat flux, E_0, and ground heat flux, G, through the energy balance equation,

$$E_0 + H_0 + G = A. \tag{1}$$

The surface latent heat flux, E_0, is determined by (Huntingford *et al.*, 1998)

$$\lambda E_0 = \frac{\lambda \rho D_c}{r_s} \tag{2}$$

where $D_c = \{q^*(T_g) - q_g\}$, T_g and q_g are surface temperature and specific humidity, respectively, q^* is the saturation specific humidity and λ is the latent heat of vaporization; ρ is the density of the air, r_s is surface resistance. Here, r_s is calculated by

$$r_s = r_{smin}/(LAI \times F1 \times F2 \times F3 \times F4 \times F5),$$

where LAI is the leaf area index and r_{smin} is the minimum value of r_s. $F1$, $F2$, $F3$, $F4$ and $F5$, whose values range between 0 and 1, represent the effects of solar radiation, soil moisture, vapour pressure deficit, air temperature and carbon dioxide, respectively. The appropriate forms of the empirical functions for $F1$–$F5$ were given by Jacquemin and Noilhan (1990).

The surface sensible heat flux, H_0, is calculated from the bulk transfer equation:

$$H_0 = \rho c_p(\theta_g - \theta_a)/R_{ah} \tag{3}$$

where c_p is the specific heat capacity of air and R_{ah} is the aerodynamic resistance of heat. θ_a is the air potential temperature at the model's first level and θ_g is the surface potential temperature. Further details on the calculation of R_{ah} can be found in Huntingford *et al.* (1998).

Finally the soil heat flux, G, is calculated from the surface energy balance equation

$$G = A - H_0 - E_0. \tag{4}$$

The surface temperature, T_g, and humidity, q_g, are predicted by a force–restore method described by Deardorff (1978). The surface radiation fluxes and surface available energy A were calculated by solving the radiation transfer equations. The radiation scheme accounts for solar position and intensity; consequently, A has a diurnal cycle and is latitude-dependent. All simulations in this study were configured to represent midlatitude summer clear-sky conditions and the position of the Sun was set to that corresponding to 12 August at 35.57°N, 104.08°E.

Two different surface vegetation distributions (see Figure 1(a) and (b)) are considered in this study, i.e. three strips aligned parallel to the y direction with the middle strip being bare soil and the other two strips covered by shrubs (hereafter three-strip type) and four-block type with two soil blocks and two shrub blocks. Note that the two surface types differ not only in pattern, but also in relative size of bare/vegetated surface, i.e. in the soil area to vegetated area ratio, R ($R = 1$ for four-block type and $R = 1/2$ for three-strip type). It should also be pointed out that we have used a homogeneous surface roughness length of 0.05 m for all simulations, since this study is focused on only effects of thermal heterogeneity. The simulations are performed over flat terrain under different geostrophic wind conditions. Combining the different surface vegetation types, wind speeds and wind directions, we performed a range of numerical experiments, with 13 of them listed in Table I (the other test experiments will be introduced in the text wherever necessary).

A 10 km deep domain is chosen for all runs and an artificial Rayleigh damping layer is added to the top half of the model domain to minimize reflection. The vertical grid is stretched and has 30 levels with a high vertical resolution of around 1.5 m near the surface for all runs. It is known that surface-energy fluxes are affected by the spatial resolution of atmospheric models (Shao *et al.*, 2001). In this study, a horizontal resolution of 500 m is adopted. Although it is still coarser than those used in LEMs, it is constrained by the computational cost on a mesoscale domain. Tian *et al.* (2003) have shown that a 0.5 km horizontal resolution is able to resolve the dominant CBL properties and convective structures. The numerical schemes used in the model are similar to those described by Clark (1977). The turbulence closure scheme used in the model is first-order and similar to that employed in large-eddy simulations (Deardorff, 1974) except that the upper limit of the mixing length scale is fixed. In the scheme, the Reynolds stress terms τ_{ij} ($i = 1, 3; j = 1, 3$) and turbulent buoyancy flux, H_i, are parametrized as:

$$\tau_{ij} = \nu S_{ij} \tag{5}$$

and

$$H_i = \nu \frac{\partial T}{\partial x_i}, \tag{6}$$

where ν is the so-called eddy viscosity and S_{ij} is the deformation tensor defined as:

$$S_{ij} = \frac{\partial U_i}{\partial x_j} + \frac{\partial U_j}{\partial x_i} - \frac{2}{3}\delta_{ij}\nabla \cdot U. \tag{7}$$

Here U is a turbulent velocity scale not the wind vector as earlier. In (5) and (6) ν is parametrized as functions of Richardson number, Ri, mixing length scale, $l(z)$, and wind shear, S, so that

$$\nu = l(z)^2 S(1 - Ri)^{1/2}, \tag{8}$$

where S is defined as,

$$S^2 \equiv \frac{1}{2} S_{ij} S_{ij}.$$

We further assume that $\nu = Ul(z)$, then following Blackadar (1962) and Mason and Sykes (1982), $l\ (z)$ is defined as:

$$\frac{1}{l(z)} = \frac{(1 - Ri)^{1/4}\phi}{\kappa(z + z_0)} + \frac{1}{l_0}, \tag{9}$$

where z is the normal distance to the surface, κ is the von Kármán constant, z_0 is the local roughness length, ϕ is the Monin–Obukhov similarity function, and l_0 is a length-scale which is fixed at 50 m.

The model horizontal domain is 90×90 km^2 for the runs listed in Table I. Periodic boundary conditions are applied at the lateral boundaries. Apart from the forcing winds and land surface properties, other parameters in the model are the same in all simulations. All three-dimensional (3D) runs are started from 0000 local time (LT) and initial profiles for 3D runs are generated by running a one-dimensional version of the model in the vertical dimension for eight hours; by that time a quasi-steady state is reached by the model (see Figure 1(c) and (d)).

Figure 2(a) shows the domain-averaged potential temperature profiles from 0010 LT to 1400 LT from the 3D experiments under the same geostrophic wind of 2 m s^{-1} over three different surface types, i.e. the all-soil surface (A02W), the all-shrub surface (V02W) and the three-strip surface (S02W). We can see that the model is capable of simulating a reasonable boundary-layer evolution. During night-time and dawn (0010 LT to 0730 LT) the temperature differences among these simulations are small and the temperature profiles near the surface are stable. A shallow unstable layer near the surface begins to develop at around 0800 LT and the nocturnal stable layer has been eroded by convection at 0900 LT. The CBL height increases with time and reaches a maximum of around 1.3 km at 1400 LT. Differences in temperature profiles between experiments with different surface types are evident from 1000 LT onwards with highest $<\theta>_{\text{domain}}$ over soil surfaces, lowest over the vegetated surfaces.

Figure 2(b) and (c) show the area-averaged potential temperature profiles over soil and vegetated surfaces from two three-strip runs with a geostrophic wind speed of 2 m s^{-1} and 10 m s^{-1}, respectively. Differences in averaged temperature profiles over three different strips can be clearly seen under a geostrophic wind speed of 2 m s^{-1} with the CBL temperature over the centre soil strip being always higher

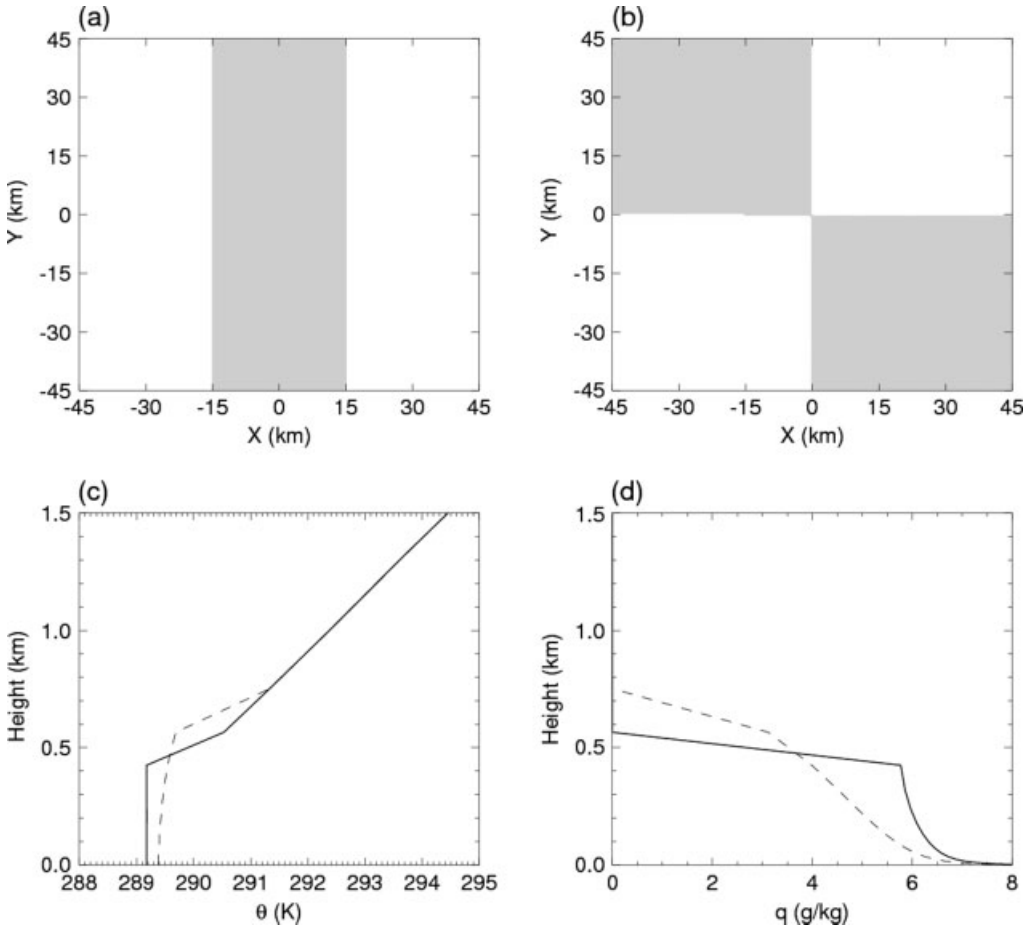

Figure 1. (a), (b) The two types of surface vegetation distribution: (a) three-strip type, (b) four-block type. White regions represent areas with shrubs; grey regions are bare soil surfaces. (c), (d) The initial profiles of (c) potential temperature and (d) humidity from two one-dimensional runs. Dashed and solid lines are for the simulation with geostrophic winds of 10 m s^{-1} and 2 m s^{-1}, respectively.

Table I. Control parameters of the numerical simulations.

Experiments	Surface styles	U_{gd} (°)	$\|U_g\|$ (m s^{-1})	Z_i (m)	H_0 (Wm^{-2})	E_0 (Wm^{-2})	W_* (m s^{-1})	t_* (s)
S02W	Three-strip	270	2	957	314	39	2.10	455
B02W	Four-block	270	2	959	319	30	2.12	452
S05W	Three-strip	270	5	982	332	38	2.16	455
S10W	Three-strip	270	10	1019	363	37	2.22	458
B10W	Four-block	270	10	1023	369	28	2.24	457
S10NW	Three-strip	315	10	991	360	37	2.20	450
B10NW	Four-block	315	10	994	365	28	2.21	449
S02N	Three-strip	0	2	958	313	39	2.11	454
S05N	Three-strip	0	5	981	332	38	2.16	454
S10N	Three-strip	0	10	1019	363	37	2.22	459
B10N	Four-block	0	10	1022	368	28	2.24	457
V02W	All shrubs	270	2	951	305	58	2.07	459
A02W	All soil	270	2	972	334	1	2.16	449

U_g and U_{gd} are geostrophic wind speed and direction, respectively. For experiment names, first letters S (three-strip), B (four-block), V (all shrubs), and A (all soil) represent surface vegetation types. The geostrophic wind speed and direction (N for 0°, W for 270°, and NW for 315°) are also embedded in the experiment names. Domain-averaged Z_i, H_0, E_0, W_*, and t_* at 1200 LT are also listed for reference.

than those over the two vegetated strips (Figure 2(b)). The temperature differences over different strips become less significant under a higher geostrophic wind of 10 m s^{-1} (Figure 2(c)). The mixed layer under higher geostrophic wind begins to develop earlier than that under weaker geostrophic wind. It is also noticeable that this occurs within a more stable profile for the higher wind case.

To further show the model's performance in simulating a reasonable surface heat flux, Figure 3 gives the time variation of the domain-averaged surface sensible heat flux and latent heat flux over homogeneous (Figure 3(a) and (c), experiments V02W and A02W) and three-strip inhomogeneous land surfaces, with different geostrophic winds (Figure 3(b) and (d), experiments S02W, S05W

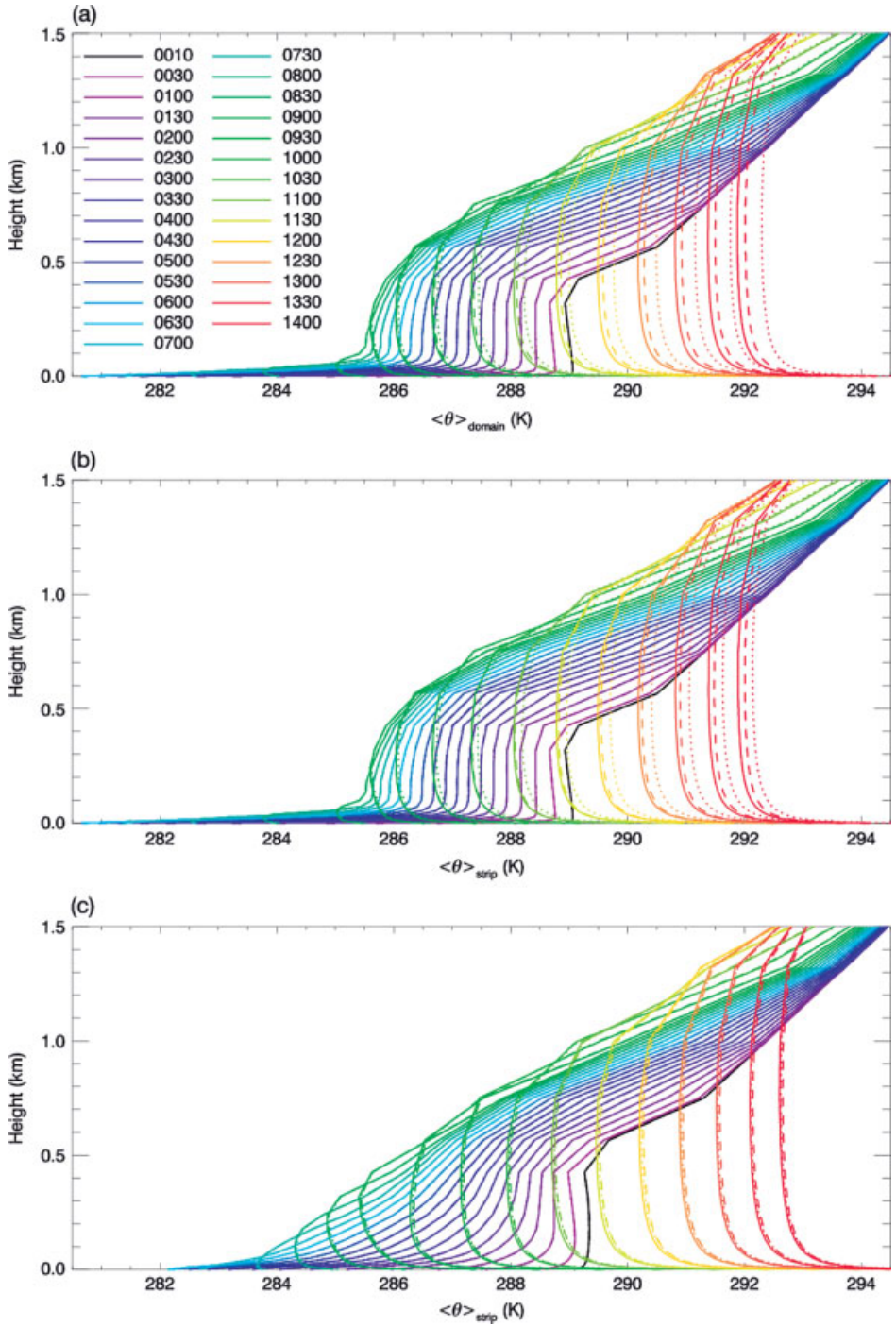

Figure 2. (a) The domain-averaged potential temperature profiles from 0010 LT to 1400 LT from experiments V02W (all shrubs, solid line), A02W (all soil, dotted line), and S02W (3-strip, dashed line). (b), (c) Area-averaged potential temperature profiles from each strip within 3-strip experiments with different winds; results are shown from over the upwind strip (solid line), the downwind strip (dashed line) and the centre strip (dotted line) for (b) S02W and (c) S10W. In all three plots the different colours represent profiles at different times as marked in panel (a).

and S10W). Also shown in Figure 3 are the normalized probability density functions (PDFs) of vertical velocity fields at 566 m above ground level (AGL) sampled from 0930 LT to 1400 LT from two experiments with homogeneous land surfaces (V02W and A02W). We can see that the time variations of the simulated surface sensible heat flux and latent heat flux are reasonable. The domain-averaged surface sensible flux becomes positive at around 0700 LT and reaches its maximum value at around 1230 LT. The surface sensible flux over the soil surface is larger than those over the vegetated surfaces, while the latent heat flux over the soil surface is smaller than those over the vegetated surfaces; consequently, the convection over the soil surface (see grey lines in Figure 3(e)) is stronger than that over the vegetated surfaces (see black lines in Figure 3(e)). Also note that even over the same land surface, the sensible heat flux and latent heat flux are slightly different under different geostrophic winds due to the fact that the net surface energy partition is dependent on the wind speed in our land surface scheme (Figure 3(b) and (d)).

Figure 3 shows that the sensible heat flux difference between the bare soil and the shrub is relatively small. This is because we selected a vegetation type of broadleaf shrubs with bare soil, therefore, the sensible heat flux over this

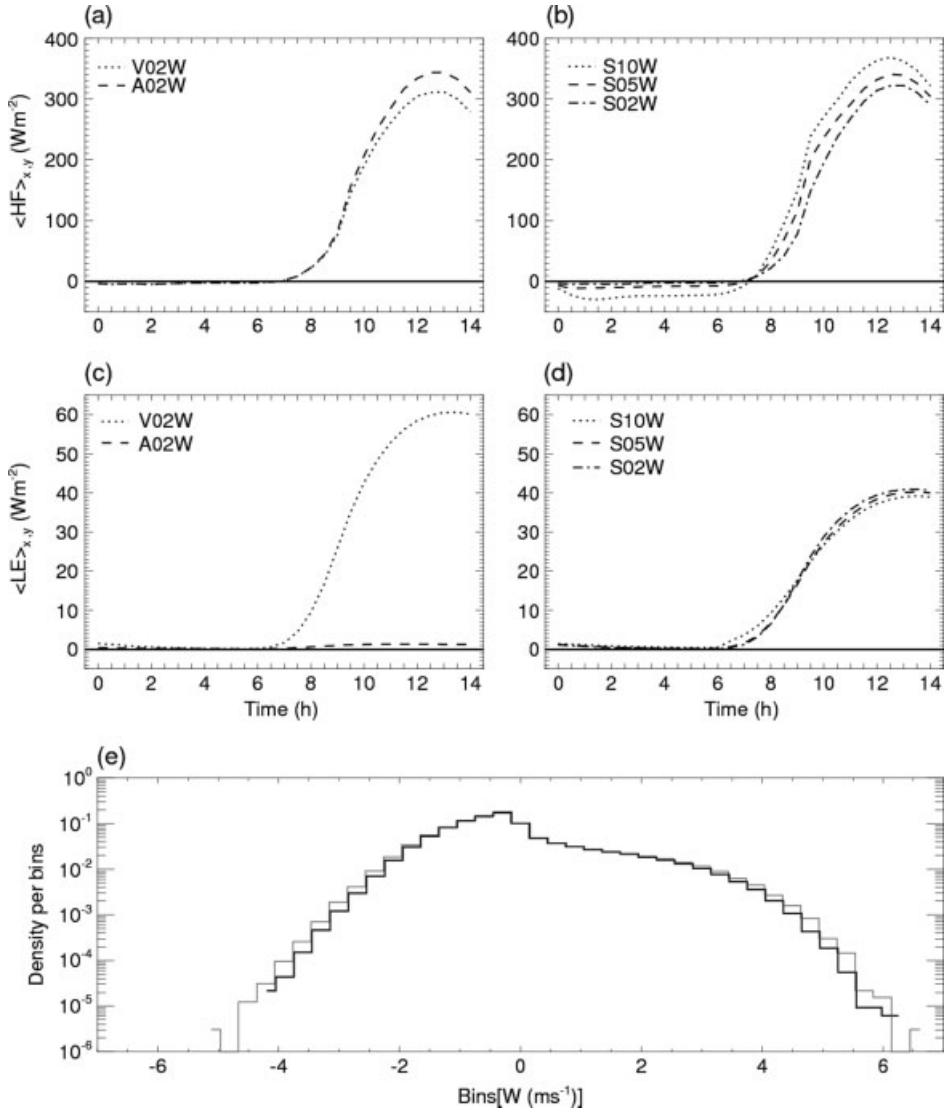

Figure 3. The time variation of domain-averaged (a), (b) surface sensible heat flux and (c), (d) latent heat flux from experiments (a), (c) V02W and A02W, (b), (d) S10W, S05W and S02W. Also shown are (e) the normalized PDFs of vertical velocity fields at 566 m AGL for the time period from 0930 LT to 1400 LT gathered from experiments V02W (black lines) and A02W (grey lines).

vegetated surface is not very large. It is worth pointing out that we have deliberately selected such a configuration in an attempt to generate a heterogeneity in the surface fluxes over an area representative of a midlatitude semi-arid region where the land surface contrasts are not very large.

3. Results

3.1. Effects on the bulk convective properties

Figure 4 shows the x–y cross-sections of the time-averaged (from 1100 LT to 1200 LT) vertical velocity fields at 566 m AGL from experiments with different surface types but the same westerly geostrophic wind of 2.0 m s^{-1} (V02W, S02W, B02W and A02W). Note that the estimated convective time-scale t_* at 1200 LT is no more than 8 minutes, therefore, a 1-hour average of the instantaneous fields is enough to eliminate random signals. In order to know whether circulations with their scales on the order of the heterogeneity scale, λ, can be caused by different scales of surface inhomogeneities, the vertical velocity w is filtered with a Butterworth filter to retain only signals with their scales greater than the heterogeneity scale, λ, and the filtered vertical velocity fields w_s are over-plotted in Figure 4. For a fair comparison, the heterogeneity scale, λ, adopted in the filter is the same for different model surfaces, i.e. λ equals 30 km. As expected, convective activities are relatively weak and uniform over the homogeneous surface compared to those over inhomogeneous surfaces (Figure 4(a) and (d)). Although small-scale convective features are overall the same over different land surfaces, the mesoscale inhomogeneity in the filtered vertical velocity fields is clearly seen in Figure 4(b) and (c) with stronger upward motions over the soil surfaces and stronger downdraughts over the areas covered with shrubs, with the vertical velocity distributions shifted slightly downwind of the surface heterogeneities. The amplitude of the filtered, mesoscale circulation is of the order of 0.5 cm s^{-1}. Note that the magnitude of the mesoscale-filtered vertical wind is simply an intensity of a few cm s^{-1}. This is consistent with the result of the LEMs study by Kang and Davis (2009) and is also supported by observations (e.g. Mahrt *et al.*, 1994; LeMone *et al.*, 2002; Kang *et al.*, 2007; Lenschow and Sun, 2007; Taylor *et al.*,

2007). However, this weak mesoscale circulation may not be considered negligible, as stressed by Ek and Mahrt (1991).

Figure 5 shows time-averaged (from 1100 LT to 1200 LT) profiles of domain-averaged vertical velocity variance, w^2, normalized by ${w_*}^2$ over the whole domain, $<w^2/{w_*}^2>_{\mathrm{domain},\,t}$, and strip-averaged w^2 normalized by the strip-averaged ${w_*}^2$, $<w^2/w_*^2>_{\mathrm{strip},\,t}$ over different strips from the three-strip experiments with a westerly geostrophic wind of 2 m s^{-1}, 5 m s^{-1}, 10 m s^{-1} (S02W, S05W and S10W). $<w^2/{w_*}^2>_{\mathrm{domain},\,t}$ is largest under a geostrophic wind of 10 m s^{-1} and is smallest under a geostrophic wind of 2 m s^{-1} (Figure 5(a)). As expected, under a geostrophic wind of 2 m s^{-1} once a well-mixed boundary layer has developed, $<w^2/{w_*}^2>_{\mathrm{strip},\,t}$ over soil surfaces is higher than that over vegetated surfaces (Figure 5(b)). Further examination of data at other times indicates that differences in $<w^2/{w_*}^2>_{\mathrm{strip},\,t}$ between soil and vegetated surface increase with time until 1200 LT or 1230 LT when surface sensible flux reaches its maximum value (not shown). The maximum differences in $<w^2/{w_*}^2>_{\mathrm{strip},\,t}$, and $<w^2/w_*^2>_{\mathrm{domain},\,t}$ are located at an altitude of half the CBL height. $<w^2/{w_*}^2>_{\mathrm{strip},\,t}$ differences between soil and vegetated surfaces become insignificant under higher geostrophic winds of 5 m s^{-1} and 10 m s^{-1} (Figure 5(c) and (d)). Overall, the results imply that the effect of heterogeneity on the CBL flow depends on geostrophic wind speed and the CBL height as well as the magnitude of the surface heat flux. Note that $<w^2/{w_*}^2>_{\mathrm{strip},\,t}$ differences between two vegetated surfaces are very small due to the horizontal advection of flux anomalies and periodical lateral boundary conditions imposed on the model domain.

Figure 6 shows the time-averaged vertical velocity fields and corresponding filtered signals from experiments over the three-strip surface with different westerly geostrophic winds of 2 m s^{-1}, 5 m s^{-1} and 10 m s^{-1}. In the early morning (averaged from 0600 LT to 0700 LT) before the surface is heated by the solar radiation, the signature of surface heterogeneities on the filtered vertical velocity fields is marginal under different geostrophic winds and signals of gravity waves are evident, particularly under higher geostrophic winds (Figure 6-1). When the CBL is well developed (from 1300 LT to 1400 LT), the effect of surface heterogeneity on convection becomes significant with the associated inhomogeneities in the filtered vertical velocity fields being most pronounced under light wind conditions (Figure 6(a)-2). Under a higher geostrophic wind of 10 m s^{-1}, the inhomogeneous patterns of the filtered vertical velocity fields exhibited in Figure 6(c)-2 are not exactly collocated with those of the surface heat flux due to strong horizontal advection. Consistent with the result in Raasch and Harbusch (2001), the effect of the surface heterogeneity on the CBL flow is still significant for a geostrophic wind of 5.0 m s^{-1} (Figure 6(b)-2). The persistent eddies on scales of order of 1 km (contour lines in Figure 6) also align with the mean wind speed and direction for strong winds (Figure 6(c)). The results here are consistent with the earlier findings by Weaver and Avissar (2001), who used a mesoscale mode over a real mesoscale domain and found that relatively weak upward motion of a few centimetres per second is located over patches of large surface heat flux with scales on the order of a few tens of kilometres. They also pointed out that the synoptic-scale wind plays a key role in orienting, steering and advecting the landscape-induced mesoscale circulations.

It is apparent that high wind speeds weaken the effect of surface heterogeneities on convective activities: the signature of the surface heterogeneity in the filtered vertical velocity field is broken under a geostrophic wind of 10 m s^{-1}, and is no longer coherently correlated to the surface inhomogeneous patterns. Figure 7 shows correlation coefficients between the anomalous vertical velocity fields ($<w>_{y,\,t}$) at 566 m AGL and the lagged surface heat flux fields ($<H_0>_{y,\,t}$) as a function of the applied lag, for inhomogeneous experiments S02W and S10W and for the two homogeneous runs A02W and V02W. Note that under a 2 m s^{-1} geostrophic wind, anomalous vertical velocity $<w>_{y,\,t}$ over the three-strip surface is clearly correlated with the surface heat flux, with an evident mesoscale pattern, with its scale in accordance with the surface heterogeneity scale (Figure 7(a)). However under a 10 m s^{-1} geostrophic wind (Figure 7(b)), there is no evidence of a correlation pattern between $<w>_{y,\,t}$ and $<H_0>_{y,\,t}$ over the three-strip surface; the correlation is almost uniform along the x direction similar to those shown for the homogeneous runs (Figure 7(c) and (d)) under a geostrophic wind of 2 m s^{-1}. Some previous studies have showed that relatively high background wind does not necessarily inhibit the mesoscale circulations, but usually advects them away, and that coherent advection of the mesoscale rolls by this wind is an important effect (Weaver and Avissar, 2001; Baidya Roy *et al.*, 2002; Weaver, 2004). Although Figure 7(b) indicates that there is no evident correlation between the mesoscale circulation and the surface heterogeneity, Figure 6(c)-2 indeed suggests that high wind tends to weaken and break up the mesoscale circulation rather than completely inhibit it.

Also note that the mesoscale inhomogeneity in the vertical velocity field is not stationary but is advected with time at the approximate background geostrophic wind (Figures 4(b),6(a)-2). The result implies that the anomalous convective activities induced by the surface heterogeneities could affect convection of the downwind area where the anomalous heat flux originates. This influence region depends on the speed of background geostrophic winds. The issue will be further discussed in section 3.2.

To examine the effect of surface heterogeneities under different wind directions, Figure 8 shows the time-averaged (from 1100 LT to 1200 LT) vertical velocity fields and corresponding filtered signals at 566 m AGL from experiments with two different surface types (three-strip and four-block) under the same geostrophic wind of 10 m s^{-1} but different wind directions (S10N, B10N, S10NW, B10NW, S10W and B10W). We can clearly see that the effects of heterogeneity on convection are sensitive to the land surface types and wind directions. For the three-strip land surface type, the wind direction dependence of the effect of heterogeneity is particularly significant, i.e. the effect of heterogeneity is most pronounced when the wind direction is parallel to the alignment (alignment here is defined as the direction along the surface patches) of the strips (Figure 8(a)), as was the case in the observational studies of Taylor *et al.* (2003, 2007). The effect of surface heterogeneity is weakest when the wind direction is perpendicular to the alignment of the strips (Figure 8(e)). For the four-block surface type, the differences in vertical velocity fields between experiments with westerly winds (Figure 8(f)) and northerly winds (Figure 8(b)) are small (as expected from symmetry arguments). The effect of surface heterogeneity for the four-block surface type is most coherent and significant under

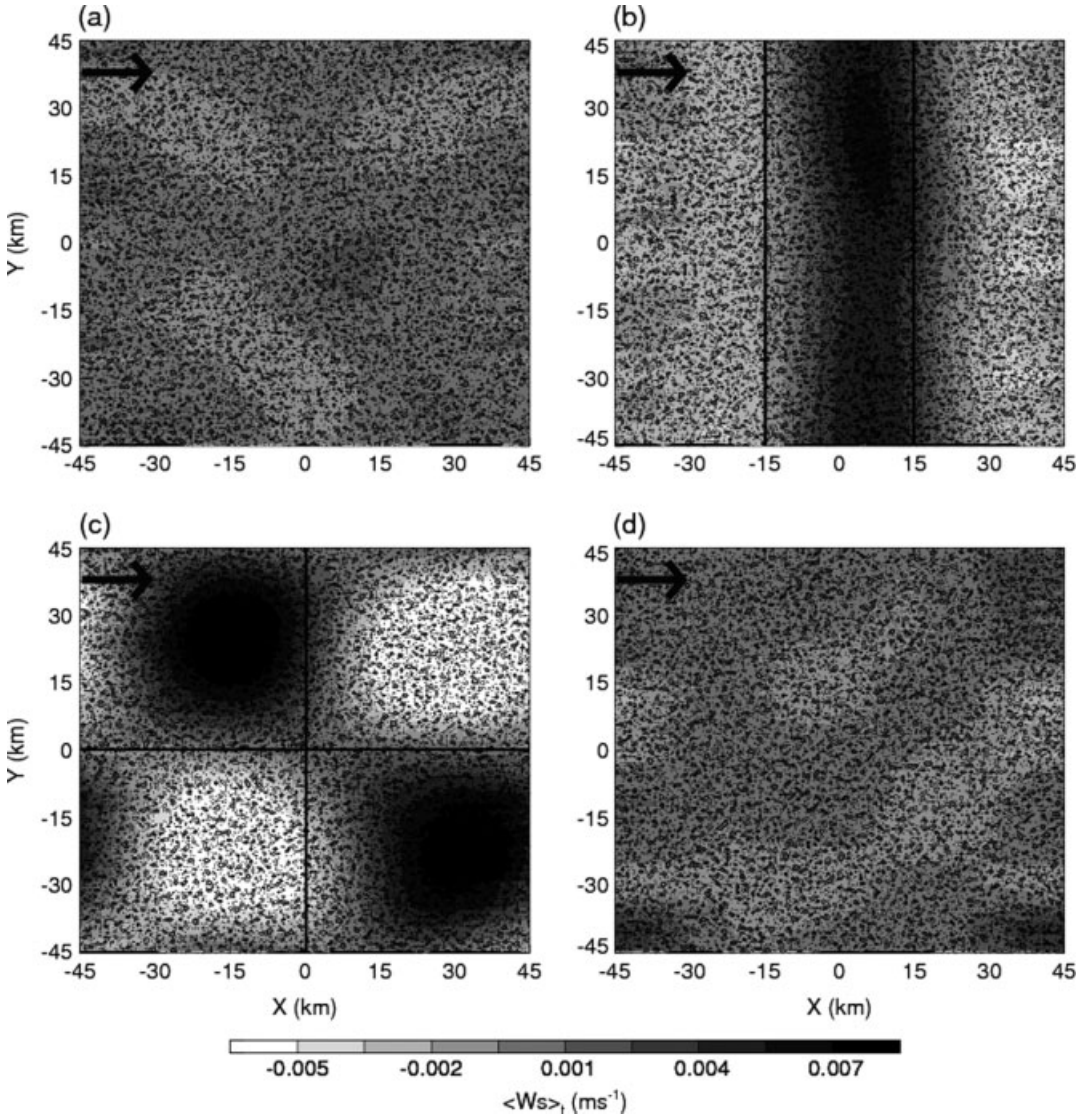

Figure 4. The x–y cross-sections of the time-averaged (from 1100 LT to 1200 LT) vertical velocity fields (line contours) at 566 m AGL from experiments with the same geostrophic wind, but different surface inhomogeneities: (a) V02W, (b) S02W, (c) B02W, and (d) A02W. Contours are at ± 1.0 and ± 0.5 m s^{-1}.The time-averaged filtered vertical velocity fields (see text for more details) are over-plotted with grey-filled contours. Geostrophic wind vectors are marked by the arrows. Straight black lines in (b), (c) delineate the pattern of the surface inhomogeneities.

northwesterly geostrophic winds (Figure 8(d)), when the effect is similar to a wind oriented parallel to a three-strip pattern.

Shen and Leclerc (1995) assumed that differences between various experimental and modelling studies on effects of heterogeneity may be attributed not only to different scales of surface inhomogeneities, but also to different wind speeds. Avissar and Schmidt (1998) showed that for larger one-dimensional inhomogeneities with scales up to 40 km even a moderate geostrophic wind of 5 m s^{-1} virtually eliminated all possible impacts of ground-surface heterogeneity on the CBL. Nevertheless, some other studies (e.g. Raasch and Harbusch, 2001) have shown that effects of heterogeneity on the CBL are still significant with geostrophic winds greater than 5 m s^{-1}, and suggested this threshold wind speed may depend on the wind direction. Our results also indicate that the effect of heterogeneity still exists under a higher geostrophic wind of 10 m s^{-1} when the wind direction is parallel to the alignment of the strips but is much less significant when wind direction is perpendicular to the alignment of the strips (Figure 8). Note that in Figure 8 and Figure 6(c)-2 the filtered vertical velocity fields are still significantly inhomogeneous under a geostrophic wind of 10 m s^{-1}; however, those inhomogeneities are incoherent and no longer clearly correlated with the surface heterogeneities as is evident in Figure 7(b).

3.2. *Effects on the CBL temperature and horizontal winds*

Figure 9 shows the vertical cross-section of $<\theta>_{y,\,t}/<\theta>_{x,\,y,\,t}$ from experiments with the three-strip surface type under different geostrophic winds (S05W, S05N, S10W and S10N) (subscript x, y of $<\theta>_{x,\,y,\,t}$ denotes that θ is averaged along the x, and y direction, subscript t denotes θ is time-averaged, here averaged from 1100 LT to 1200 LT). The variations of $<\theta>_{y,\,t}/<\theta>_{x,\,y,\,t}$ along the x direction, i.e. the direction across the alignment of the three surface strips (as defined before), are different under different geostrophic winds and at different heights. Note that within the CBL, the $<\theta>_{y,\,t}/<\theta>_{x,\,y,\,t}$ ratio over the soil surface is higher than elsewhere in all four cases. The temperature differences between the soil and vegetated surfaces decrease with height

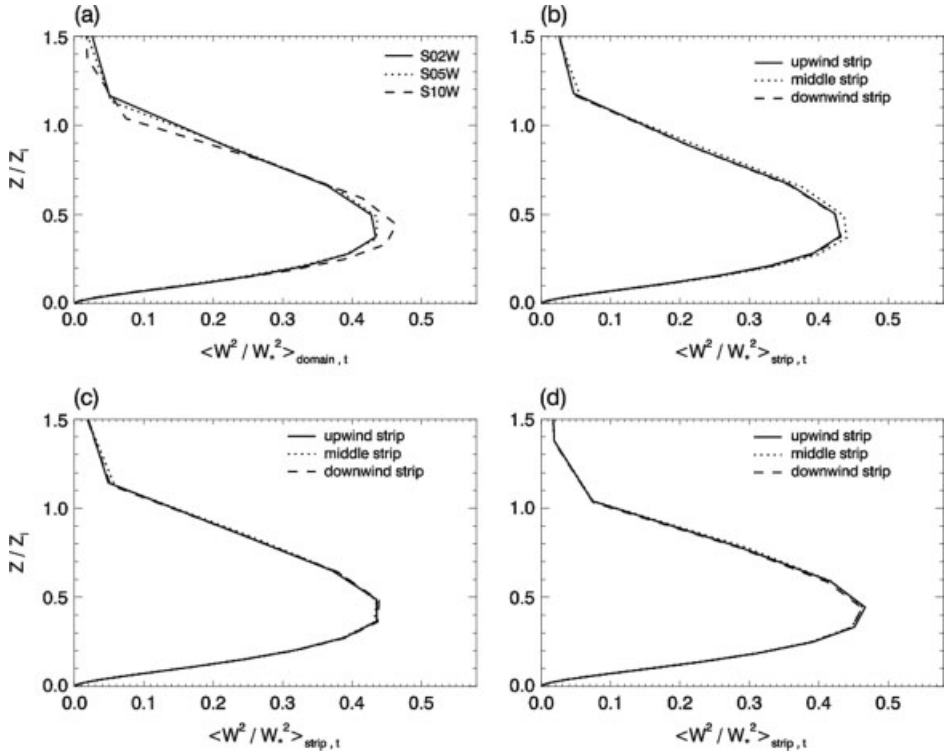

Figure 5. The time-averaged (from 1100 LT to 1200 LT) profiles of (a) domain-averaged w^2 normalized by the domain-averaged ${w_*}^2$, and (b), (c), (d) strip-averaged w^2 normalized by the strip-averaged ${w_*}^2$ from experiments with three-strip surface, but different geostrophic winds: (b) S02W, (c) S05W, and (d) S10W.

in the CBL. $<\theta>_{y,\,t}$ near the model soil surface is about 0.3–0.6 K higher than elsewhere in Figure 9. Using an LEM, Górska *et al.* (2008) simulated a temperature difference of 0.7 K over a heterogeneous surface with a heat flux contrast of 40 W m^{-2}. Figure 3 indicates that heat flux contrast between soil and vegetated surface is about 30 W m^{-2} in our study. It is apparent that the simulated temperature differences in Figure 9 are reasonable compared to that in Górska *et al.* (2008).

It is apparent that the effect of heterogeneity on $<\theta>_{y,\,t}$ still exists above the CBL top even under a geostrophic wind of 10 m s^{-1}. Wieringa (1986) pointed out that when the dominant scale of the surface inhomogeneities is small enough, the flow above a certain height becomes independent of a position, i.e. the flow becomes pseudo-homogeneous. This is because the long time-scale eddies above this height will not have sufficient time to adjust to the changing surface. Hopwood (1995) used tethered–balloon data collected over an inhomogeneous semi-rural area (with heterogeneity scales on the order of no more than 10 km) to investigate perturbations caused by surface inhomogeneities and deduced that 100 m is the height at which perturbations introduced into the flow by surface inhomogeneities have diffused into the flow interior. The heterogeneity effect on the temperature is the reverse of that in the CBL between 1.3 and 2.6 Z_i for a 5 m s^{-1} northerly geostrophic wind (Figure 9(b)) and between 1.3 and 2.3 Z_i for a 10 m s^{-1} northerly geostrophic wind (Figure 9(d)). For westerly geostrophic winds the effects are less clear but are approximately between 1.3 and 2.4 Z_i for a 5 m s^{-1} wind and 1.3 and 2.2 Z_i for a 10 m s^{-1} wind, with the sloping contours in Figure 9(c) suggestive of a gravity wave impact. The result therefore suggests that the top of this layer with reversed temperature effects decreases with increasing geostrophic wind speed.

Theoretically, Wood and Mason (1991) proposed a thermal blending height formula which links the horizontal length-scale of surface heterogeneity (λ) to the height (Z_h) where surface heterogeneity has an influence on the flow, i.e.,

$$\lambda = Z_h\,(C_{th}\,U\,\theta_v)/\overline{w'\theta'}, \tag{10}$$

here, $C_{th} = 3.1 \times 10^{-3}$ is a non-dimensional coefficient (Mahrt, 2000), U is the mean horizontal wind, θ_v is the mean virtual potential temperature and $\overline{w'\theta'}$ is the spatially-averaged surface heat flux. Using the surface heat flux data at 1200 LT from the three-strip experiments with a westerly geostrophic wind of 2 m s^{-1}, 5 m s^{-1} and 10 m s^{-1} (see Table I), the estimated Z_h is 2.7 Z_i, 2.4 Z_i and 1.8 Z_i, respectively. Note that the above estimated Z_h values are close to that inferred from the model results analysed above, and they are overall consistent in the aspect that the height at which the effect of heterogeneity temperatures vanishes decreases with geostrophic wind speed and is dependent on the magnitudes of the surface heat flux as well as the scale of surface heterogeneities. Kang *et al.* (2007) found that the blending height of the surface heterogeneity likely exceeds the atmospheric boundary layer (ABL) depth, but the estimated Z_h from our simulations is far above the boundary-layer height. It is possible that this departure is due to the fact that the value of C_{th} given by Mahrt (2000) does not exactly fit the conditions in our runs.

Contrasts in the surface heat flux also have a significant impact on the winds, and this impact is also sensitive to geostrophic wind speeds and wind directions. Figure 10 gives the spatially (along y direction) and time-averaged

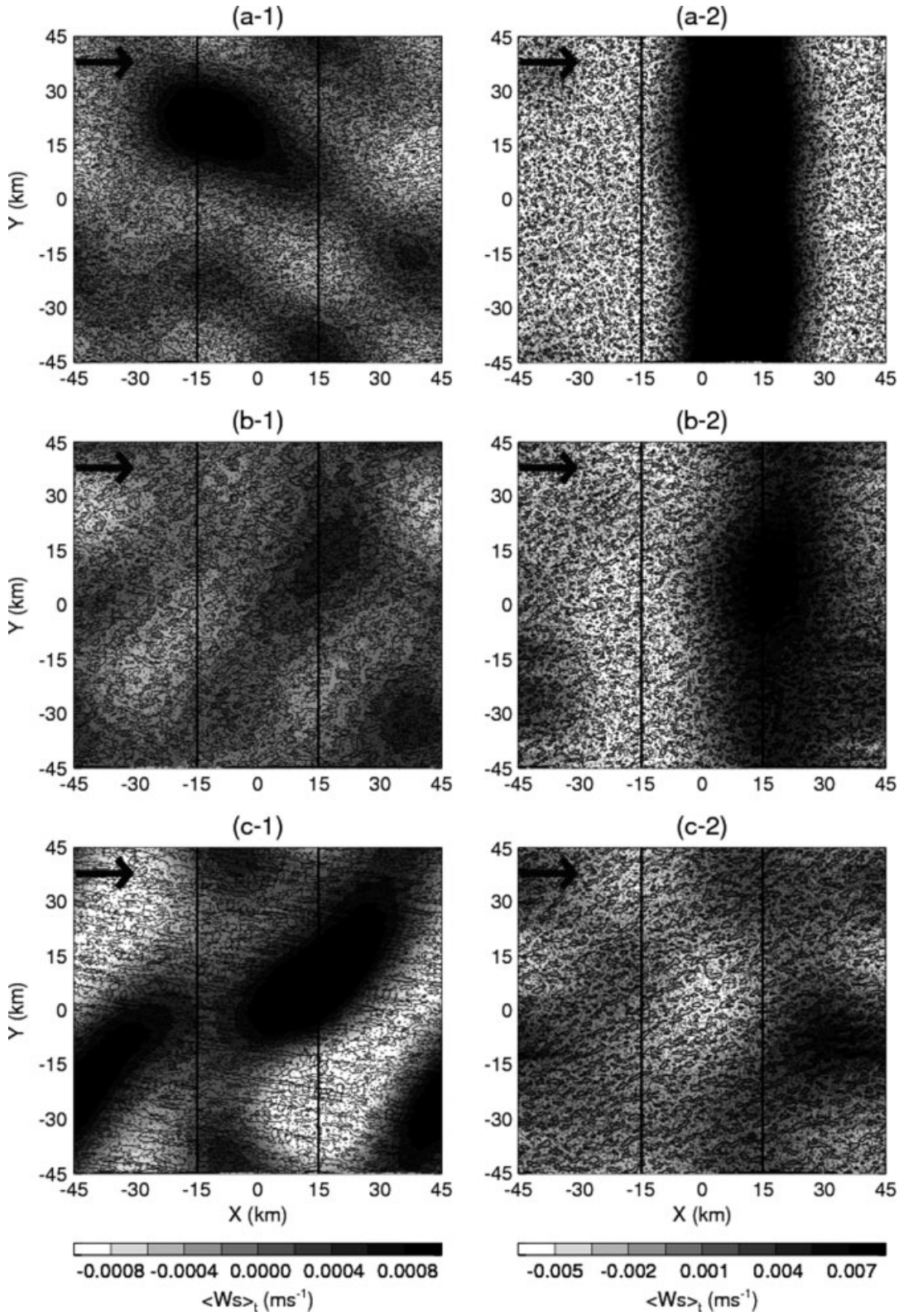

Figure 6. The x–y cross-sections of the time-averaged vertical velocity fields (line contours) from the three-strip experiments with the various geostrophic winds (a) S02W, (b) S05W, and (c) S10W. (1) is averaged from 0600 LT to 0700 LT at 132 m AGL and (2) is averaged from 1300 LT to 1400 LT at 566 m AGL. Contours are at ± 0.01 and ± 0.05 m s^{-1} in (1) and ± 1.0 and ± 0.5 m s^{-1} in (2). The time-averaged filtered vertical velocity fields (see text for more details) are over-plotted with grey-filled contours. Geostrophic wind vectors are marked by the arrows. Straight black lines in (1) and (2) delineate the pattern of the surface inhomogeneities.

(from 1100 LT to 1200 LT) velocities $<u'>_{y,\,t}$, $<w>_{y,\,t}$, $<w^2>_{y,\,t}$ and filtered vertical velocities $<w_s>_{y,\,t}$ from experiments with the three-strip surface type under westerly and northerly geostrophic winds of 10 m s^{-1} (S10W and S10N). Here, the perturbation u' is calculated from u with the mean wind removed. The wind fields in experiment S10W are quite different from those in experiment S10N along the x direction (Figure 10-1). Under a 10 m s^{-1} westerly geostrophic wind, the strongest westerly perturbation $<u'>_{y,\,t}$ within the CBL is over the middle soil strip

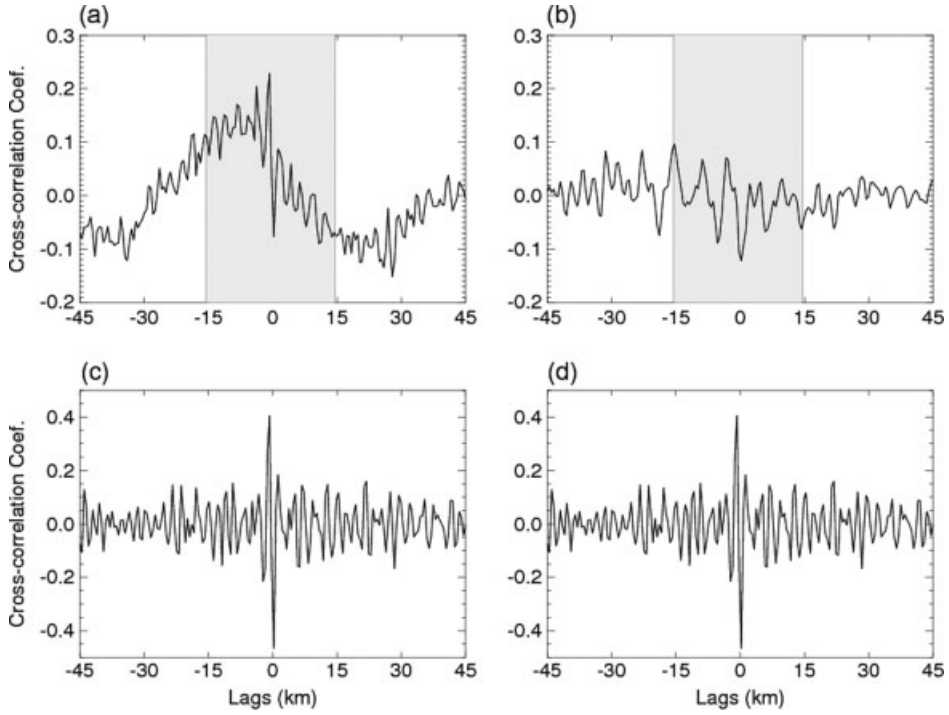

Figure 7. Cross-correlation analysis between the time-averaged (from 1300 LT to 1400 LT) anomalous vertical velocity fields $<w>_{y,\,t}$ at 566 m AGL and lagged surface heat flux $<H_0>_{y,\,t}$ from experiments (a) S02W, (b) S10W, (c) V02W, and (d) A02W, each shown as a function of the applied lag. Regions within the middle soil strip are shaded in (a) and (b).

and in the downwind interface ($x = 15$ km) of two strips (Figure 10(a)-1). Under a 10 m s^{-1} northerly geostrophic wind, the strongest westerly perturbation $<u'>_{y,\,t}$ is close to the western interface ($x = -15$ km) of two strips, while the strongest easterly perturbation $<u'>_{y,\,t}$ is close to the eastern interface of two strips ($x = 15$ km) (Figure 10(b)-1). The horizontal wind differences are related to the secondary horizontal circulation induced by the vertical velocity difference between warm and cold patches. Under a 10 m s^{-1} northerly geostrophic wind, the associated weak westerly wind in the boundary layer may also interact with the secondary circulations induced by surface inhomogeneities for the three-strip surface type (Figure 10(b)-1); consequently, the westerly perturbations $<u'>_{y,\,t}$ are positive near the western interface ($x = -15$ km) and negative near the eastern interface of two strips ($x = 15$ km) in the lower CBL.

For a layer between approximately 0.8 and 2.0 Z_i the westerly wind perturbations $<u'>_{y,\,t}$ have reversed signs compared with those below (Figure 10-1), consistent with the temperature effects shown in Figure 9. Under a 10 m s^{-1} westerly geostrophic wind, within the CBL a displacement of maximum $<u'>_{y,\,t}$ and $<w^2>_{y,\,t}$ from the warm surface to downwind can be noted (Figure 10(a)-1 and 10(a)-4). With this westerly wind, above the CBL inclined structures in the horizontal winds are clearly evident, suggestive of gravity wave effects.

Within the CBL, $<w>_{y,\,t}$ is greater on the downwind side ($x = 10$ km) of the soil strip than the upwind side under a 10 m s^{-1} westerly geostrophic wind (Figure 10(a)-2). Under a 10 m s^{-1} northerly geostrophic wind the effects of the surface heterogeneity are much more significant, with greater $<w>_{y,\,t}$ over the soil strip and at its boundaries (Figure 10(b)-2). The vertical velocity variance, $<w^2>_{y,\,t}$, in the middle of the CBL over the soil strip is slightly higher than that over vegetated strips in both wind conditions, but this is shifted downwind with a westerly geostrophic wind (Figure 10-4). The mesoscale pattern in filtered vertical velocity, $<w_s>_{y,\,t}$, is quite different under different wind directions. Consistent with the earlier discussions, the mesoscale circulation under a 10 m s^{-1} westerly geostrophic wind is weaker and less coherent, but still exists. Under a 10 m s^{-1} northerly geostrophic wind, the mesoscale circulation is much more significant and almost collocated with the surface heterogeneity pattern. The vertical mesoscale circulation is coherent over a depth from the surface to approximately 1.3 Z_i (Figure 10-3), which is approximately the depth of the deepest CBL eddies (Figure 10-4).

Figure 11 further shows the corresponding $<u'>_{y,\,t}$, $<w>_{y,\,t}$, $<w^2>_{y,\,t}$ and filtered vertical velocities $<w_s>_{y,\,t}$ from experiments with the three-strip surface type under light westerly and northerly geostrophic winds of 2 m s^{-1} (S02W and S02N). Under a light westerly geostrophic wind of 2 m s^{-1}, in contrast to the results under a higher westerly geostrophic wind of 10 m s^{-1}, the mesoscale pattern in $<u'>_{y,\,t}$ along the x direction is more pronounced with $<u'>_{y,\,t}$ over the upwind strip being higher than that over the downwind strip (Figure 11(a)-1). Consistent with the features in Figure 4(b), $<w_s>_{y,\,t}$ and $<w^2>_{y,\,t}$ over the soil strip are much higher than over the vegetated surfaces (Figure 11(a)-3 and 11(a)-4). $<u'>_{y,\,t}$ variations along the x direction under a northerly geostrophic wind of 2 m s^{-1} are similar to those under a northerly geostrophic wind of 10 m s^{-1} (Figure 11(b)-1). However, Figure 11(b)-3 and 11(b)-4 indicate that under a light northerly wind of 2 m s^{-1}, maximum $<w_s>_{y,\,t}$ and $<w^2>_{y,\,t}$ occur over the middle soil strip, while under a northerly wind of 10 m s^{-1}, maximum $<w_s>_{y,\,t}$ and $<w^2>_{y,\,t}$ regions are shifted slightly towards the eastern edge of the middle soil strip (Figure 10(b)-3 and 10(b)-4).

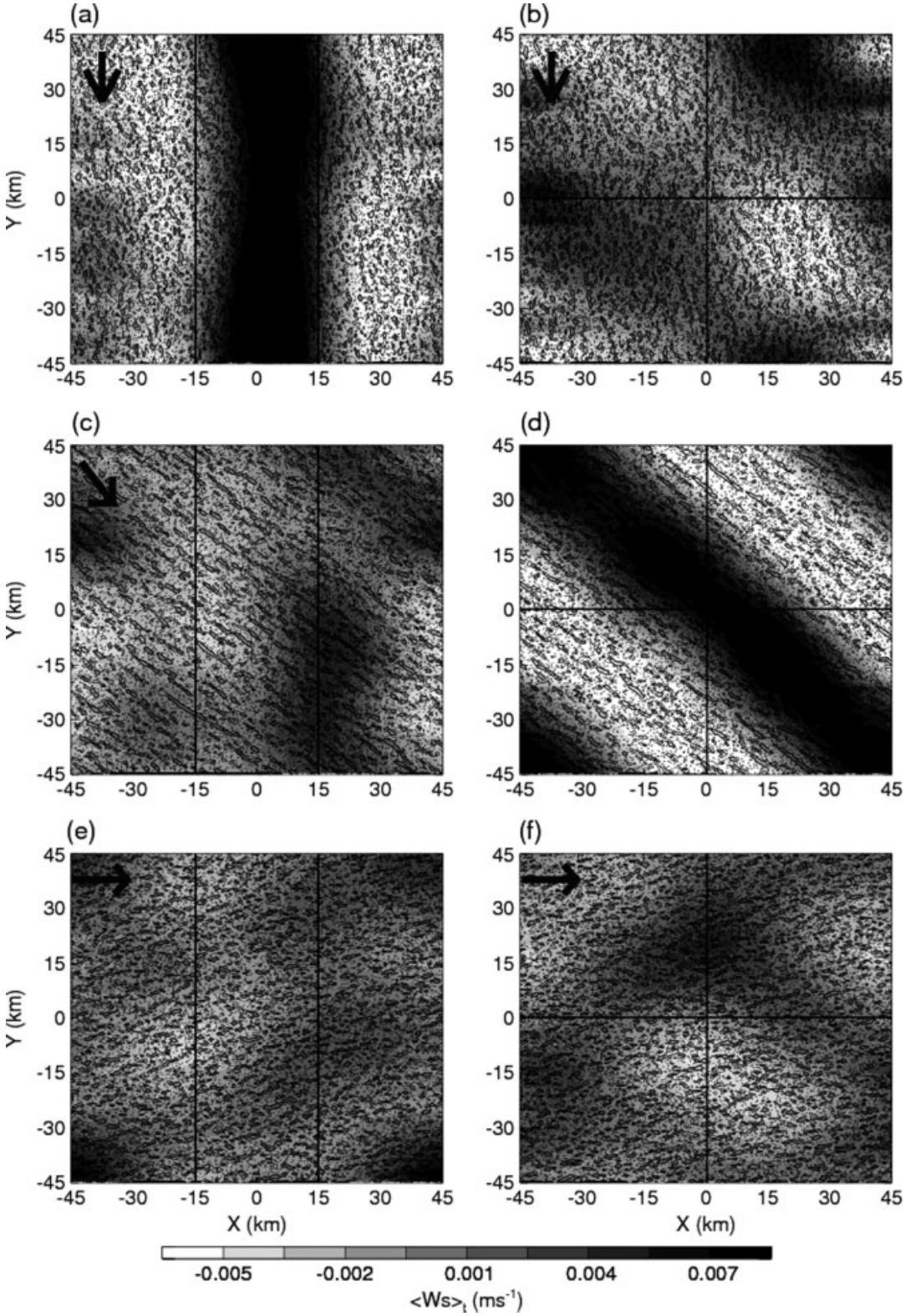

Figure 8. As Figure 4, but from three-strips and block pattern experiments using 10 m s^{-1} geostrophic winds from the north, north-west or west: (a) S10N, (b) B10N, (c) S10NW, (d) B10NW, (e) S10W, and (f) B10W.

We can infer from Figure 9 to Figure 11 that the height above which the heterogeneity effects on vertical motions tend to vanish is well above the CBL top. Figures 10 and 11 clearly show a convergence towards the warm surface in the CBL and a divergence near the top of the CBL that reaches up to approximately 2.5 Z_i. Like the convergence, this divergence is associated with temperature and vertical velocity differences and is an effect of the surface heterogeneities. Above this point, the level above which the heterogeneity effects on vertical motions tend to vanish can reach 3.3 Z_i under the lighter geostrophic wind of 2 m s^{-1} (Figure 11-1). For higher westerly geostrophic winds of 10 m s^{-1} the effects become more complex, with the inclined structures above the CBL again suggestive of gravity waves reaching at least 4 Z_i (Figure 10(a)-1).

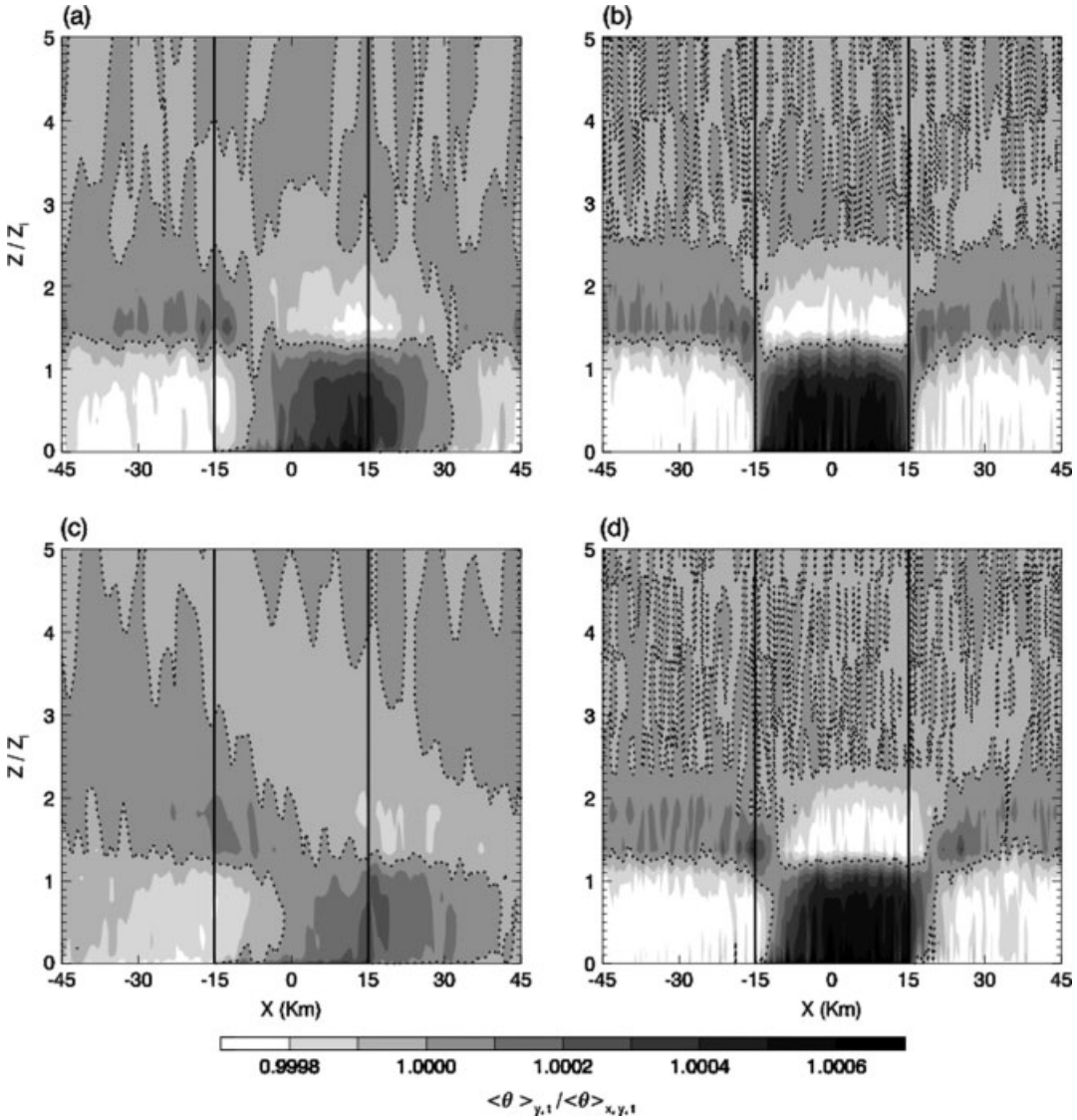

Figure 9. The vertical cross-sections of spatially (along y direction) and time-averaged (from 1100 LT to 1200 LT) $<\theta>_{y,t}/<\theta>_{x,y,t}$ from three-strip experiments using varying geostrophic winds (a) S05W, (b) S05N, (c) S10W, and (d) S10N. Dotted lines delineate where $<\theta>_{y,t}/<\theta>_{x,y,t}$ equals 1. Straight black lines in each panel delineate the pattern of the surface inhomogeneities.

We know that the contrast in the surface heat flux will induce secondary circulations which are generally characterized by the low-level air flowing from a cooler surface to a warmer surface. We can see from Figure 9 that the CBL temperatures over soil surfaces are higher than those over vegetated surfaces, while the signals in filtered vertical velocities show clear mesoscale anomalies collocated with surface heterogeneities under reasonably light wind conditions. Secondary circulations induced by those contrasts in the CBL temperatures can also affect the intensity of convection (Yi *et al.*, 2000). A recent theoretical study by Baldi *et al.* (2008) showed that land surface variability generates available potential energy and can make the environment of the lower troposphere more favourable to cloud formation. The heterogeneity effect on initiation of convection will be further discussed in the next section.

4. Heterogeneity effect on initiation of convection

The interaction between the boundary-layer convection and the mesoscale secondary circulations induced by the surface heterogeneities has implications for the initiation of deep moist convection. Weaver (2004) found that the strong vertical motions associated with mesoscale circulations can trigger shallow or even deep convection. Mesoscale circulations can lift the 'lid' of convective inhibition at the top of the boundary layer (e.g. Morcrette *et al.*, 2007). Pre-moistening of the free troposphere in such regions may then favour subsequent convective clouds. The clouds themselves are fed by convective updraughts of high equivalent potential temperature (θ_e) air embedded within the much weaker mesoscale circulations and there is evidence that the maximum values of θ_e found in these updraughts, rather than the mean θ_e of the boundary layer, can significantly influence the timing of the initiation of convection (Weckwerth, 2000). Cloud physics are not explicitly simulated within the model used in this study, and the heterogeneity effect on moist convective processes is not addressed in detail. However, some useful information on the potential for the initiation of deep convection can still be gained from combined diagnostics of the vertical velocity and θ_e. In particular, in this section we examine both the

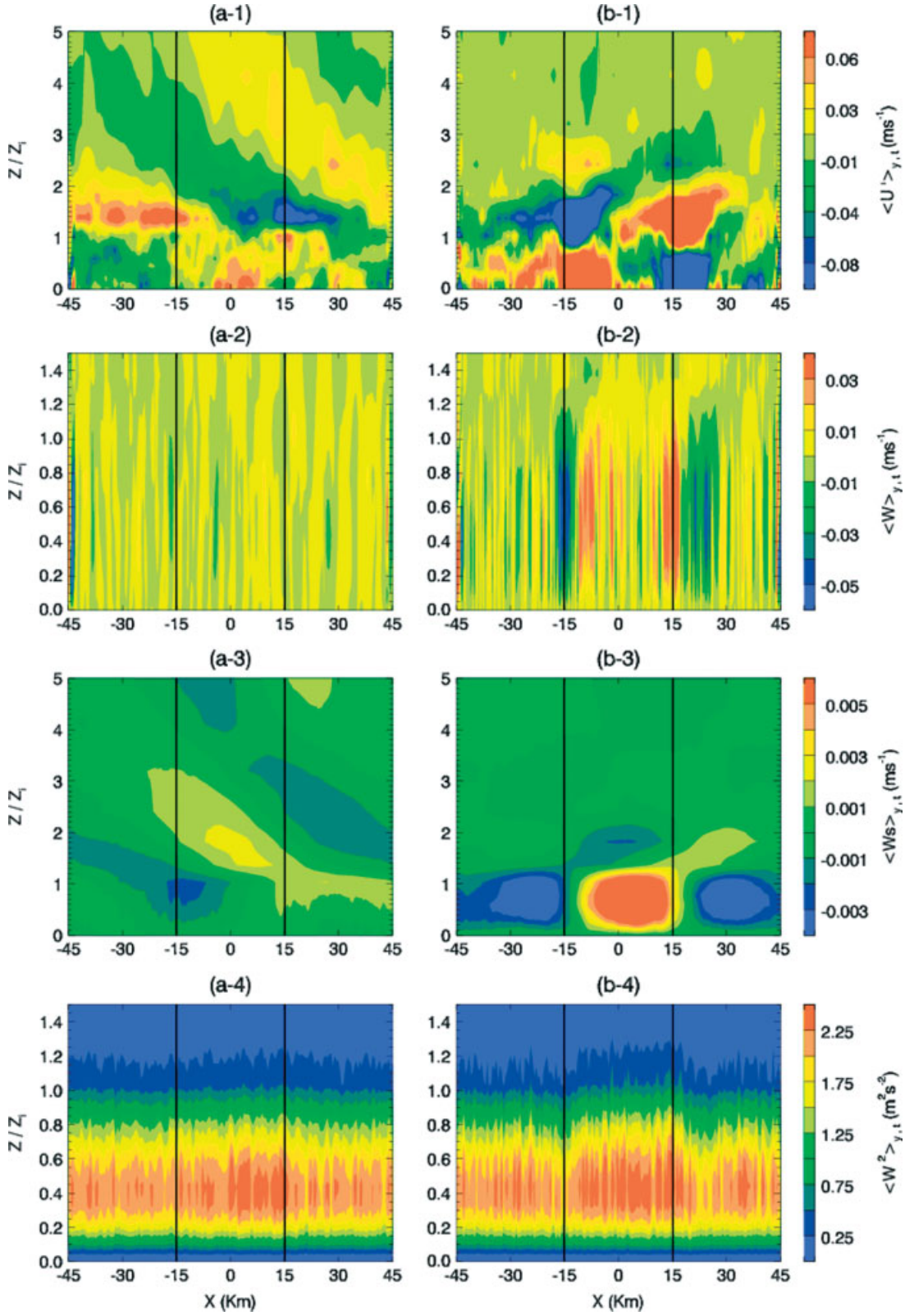

Figure 10. The vertical cross-sections of spatially (along y direction) and time-averaged (from 1100 LT to 1200 LT) velocities (1) $<u'>_{y,t}$, (2) $<w>_{y,t}$, (3) $<w_s>_{y,t}$, and (4) $<w^2>_{y,t}$ from three-strip experiments (a) S10W, and (b) S10N. w_s is filtered vertical velocity. Straight black lines in each panel delineate the pattern of the surface inhomogeneities.

mesoscale circulations and the high-θ_e updraughts that feed convective clouds themselves.

When the geostrophic wind has the same direction as that of the secondary circulation induced by the surface flux contrast, the mesoscale uplift tends to be suppressed by the geostrophic wind. However, when the geostrophic wind opposes the secondary circulation, the convergence is strengthened (e.g. Segal and Arritt, 1992).

In order to examine the spatial variation in the frequency of occurrence of high-θ_e updraughts that could trigger deep convection, Figure 12 shows vertical cross-sections of the 10th percentile of the vertical velocity and the equivalent

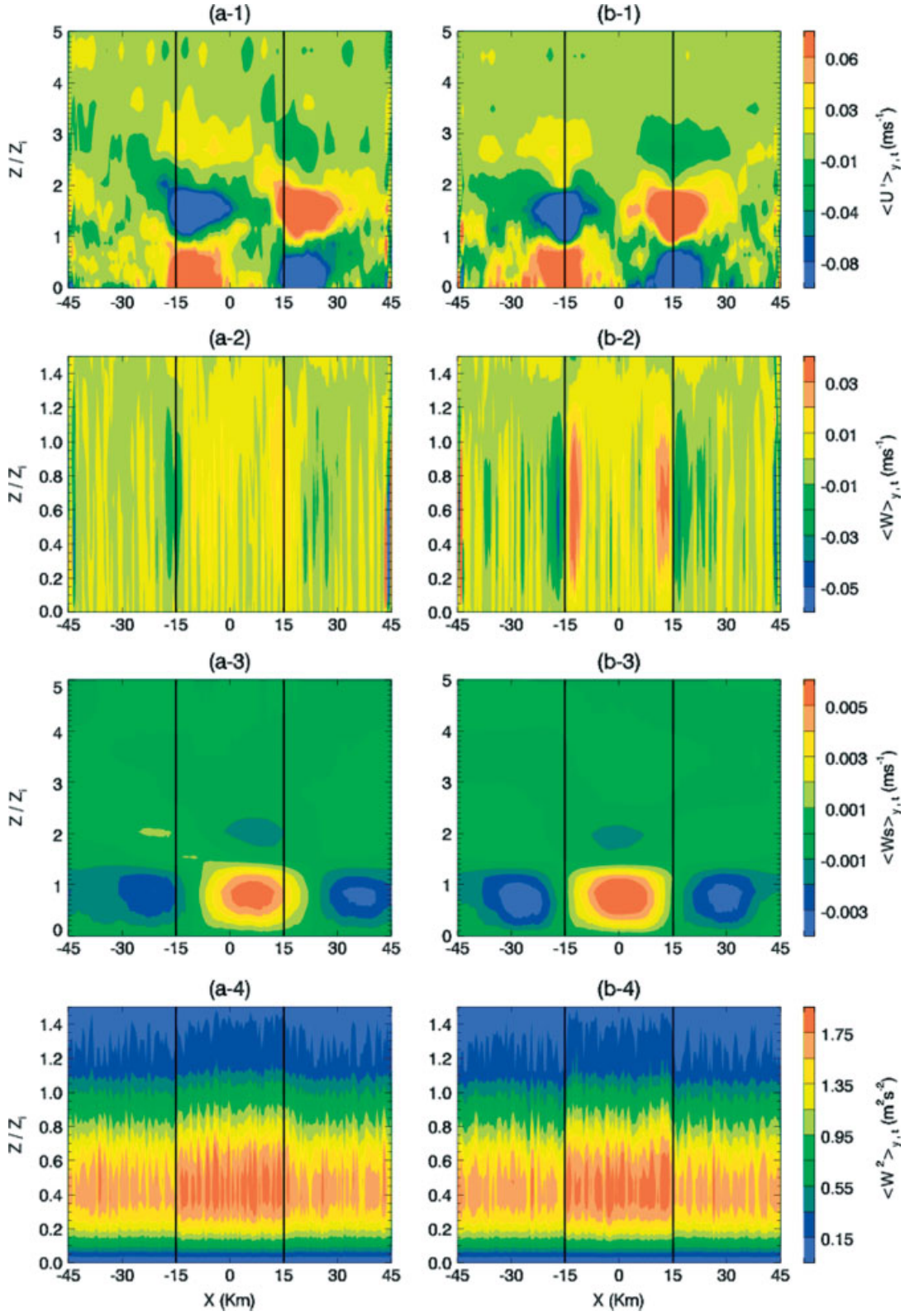

Figure 11. As Figure 10, but for experiments (a) S02W, and (b) S02N.

potential temperature in the three-strip experiments with westerly and northerly geostrophic winds of 2 m s^{-1}. The samples are gathered within the CBL from 1100 LT to 1200 LT, using all data from along the y direction for each x location. Under a 2 m s^{-1} westerly wind, we can see that the highest θ_e and vertical velocities occur at the eastern, downwind edge of the middle soil strip in the CBL (Figure 12-1). Under a northerly geostrophic wind of 2 m s^{-1}, highest θ_e and vertical velocities tend to occur over the middle soil strip in the CBL (Figure 12-2).

The results in Figure 12 are in accordance with those in Figure 11. Under light westerly geostrophic winds, the mesoscale circulation on the eastern side of the soil strip opposes the ambient geostrophic wind and, through nonlinear effects, leads to a stronger convergence zone over the downwind edge of the middle soil strip. The maximum

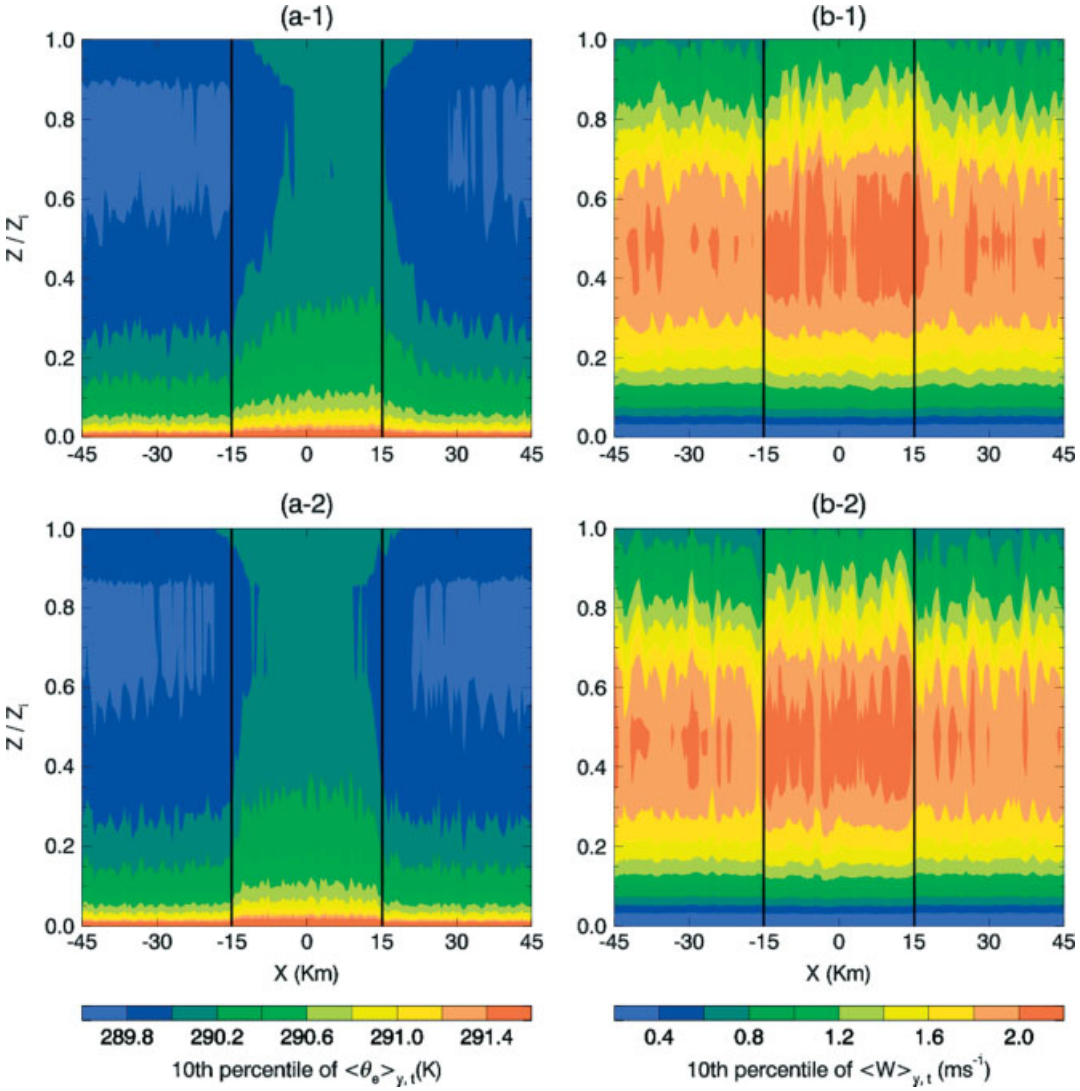

Figure 12. Vertical cross-sections of the 10th percentile of (a) the equivalent potential temperature and (b) the vertical velocity in the three-strip experiment (1) S02W, and (2) S02N. The samples are gathered from 1100 LT to 1200 LT along the *y* direction. Straight black lines in each panel delineate the pattern of the surface inhomogeneities.

convective updraughts are found at this location. Under northerly light geostrophic winds, there is very little ambient wind in the *x* direction and therefore very limited interaction between the secondary circulation and the ambient wind; therefore highest θ_e and vertical velocities are over the middle soil strip due to higher surface heat flux.

Figure 13 is similar to Figure 12, showing the 10th percentile of the vertical velocity and the equivalent potential temperature in the three-strip experiment, but for a higher geostrophic wind of 10 m s^{-1} rather than 2 m s^{-1}. Consistent with results under light westerly geostrophic winds, we can see that strongest vertical velocities and highest θ_e tend to occur at the downwind area of the middle soil strip in the CBL under a 10 m s^{-1} westerly geostrophic wind. In contrast to Figure 12-2, strongest vertical velocities and highest θ_e in the experiment with a northerly geostrophic wind of 10 m s^{-1} also tend to occur at the eastern area of the middle soil strip in the CBL.

The results here suggest that under reasonable light northerly winds the favourable location of deep convective initiation is over the middle soil strip and under reasonable light westerly winds the favourable location for triggering shallow or even deep convection tends to be downwind of the middle soil strip. When the geostrophic wind increases, under both the westerly and northerly wind conditions, strongest vertical velocities and highest θ_e are located at the eastern area of the middle soil strip where the deep convection is most likely to be triggered. It is possible that this effect is due to the westerly advection of the mesoscale convergence zone, slightly eastward over the relatively hot soil, providing the right conditions for strong updraughts.

5. Summary and conclusion

Through a series of idealised model simulations, the effects of heterogeneity on convective properties over a mesoscale flat domain with different distributions of surface fluxes, as a result of different distributions of soil and vegetation areas, are investigated systematically. Effects of surface type on surface roughness were neglected, to allow surface-flux effects to be studied in isolation. The modulation of the effects of heterogeneity by various geostrophic wind speeds and directions is examined and compared with the corresponding results obtained from previous published LEM studies over small-scale domains. Our results indicate that the effect of heterogeneity is still detectable at

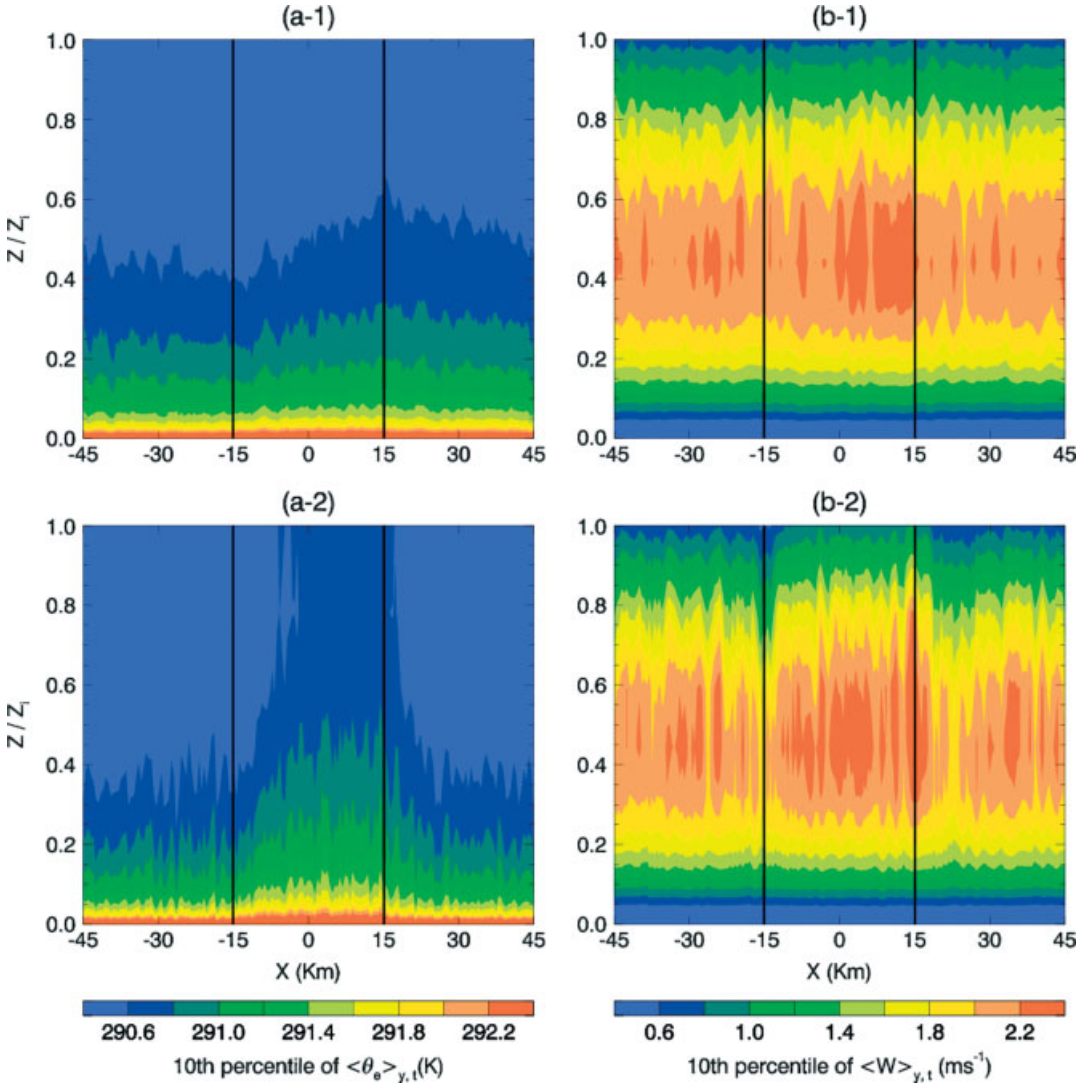

Figure 13. As Figure 12, but experiments for (1) S10W, and (2) S10N.

a high geostrophic wind of 10 m s^{-1}. Consistent with previous results, our analysis shows that the effect of surface heterogeneities on convective properties is height-dependent and most significant within the lower CBL. The height at which the heterogeneity effects on potential temperature and winds become insignificant is well above the CBL top. With light geostrophic winds the effects reach to at least 3.3 Z_i, but the details depend on the wind speed and directions as well as the orientation of surface heterogeneities.

Within the CBL the surface heat flux contrast has a complex impact on horizontal momentum distributions and the effect is closely related to the geostrophic wind speed and direction as well as the alignment of the surface heterogeneities. A mesoscale pattern in the vertical velocity field, as well as horizontal winds, is collocated with the surface heterogeneities under light geostrophic winds and moves with the CBL winds under higher geostrophic winds. When the geostrophic wind direction is perpendicular to the alignment of the surface heterogeneities over a three-strip surface type, the mesoscale pattern in horizontal velocity is more pronounced with significant variations in the wind components at the interfaces between two different surface patches. Under light geostrophic wind speeds, the interaction between the CBL background winds and the secondary circulation induced by contrasts in the surface heat flux may be another mechanism for the wind direction dependence of the heterogeneity effect.

The interaction between the secondary circulation and the geostrophic flow causes convergences at the interfaces between different land patches. The vertical motions associated with these convergence zones, which may favour deep convective systems under favourable conditions (e.g. Cheng and Cotton, 2004; Childs *et al.*, 2006), can have an important effect on convection development. The intensity of the convergence zone associated with the secondary circulation and the background wind should depend on the balance of the geostrophic wind speed and strengths of the secondary circulation, and the strongest convergence forms when the strength of the secondary circulation is balanced by the geostrophic winds. Due to this effect, under reasonably light geostrophic winds, the interaction between background winds and the secondary circulations favours convective initiation at the downwind (eastern) edge of the middle soil strip when (westerly) geostrophic winds are perpendicular to the alignment of the surface heterogeneities, since the greatest mesoscale ascent, maximum updraughts and maximum values of θ_e are found there.

Acknowledgements

This work is supported by National Basic Research Program of China (2006CB400501, 2010CB428604) and National Science Foundation of China (40730949). We would also like to thank the New Century Young Scientists Project of the Education Ministry of China for their support. The BLASIUS model is provided by the Met Office, United Kingdom. We also thank Andy Brown and Andy Ross for BLASIUS support and three anonymous reviewers for their helpful comments.

References

Albertson JD, Kustas WP, Scanlon TM. 2001. Large-eddy simulation over heterogeneous terrain with remotely sensed land surface conditions. *Water Resour. Res.* **37**: 1939–1953.

André J-C, Bougeault P, Goutorbe J-P. 1990. Regional estimates of heat and evaporation fluxes over non-homogeneous terrain. Examples from the HAPEX-MOBILHY programme. *Boundary-Layer Meteorol.* **50**: 77–108.

Avissar R, Schmidt T. 1998. An evaluation of the scale at which ground-surface heat flux patchiness affects the convective boundary layer using large-eddy simulations. *J. Atmos. Sci.* **55**: 2666–2689.

Baidya Roy S, Avissar R. 2000. Scales of response of the convective boundary layer to land-surface heterogeneity. *Geophys. Res. Lett.* **27**: 533–536.

Baidya Roy S, Avissar R. 2002. Impact of land use/land cover change on regional hydrometeorology in Amazonia. *J. Geophys. Res.* **107**: D20, DOI: 10.1029/2000JD000266.

Baidya Roy S, Weaver CP, Nolan DS, Avissar R. 2003. A preferred scale for landscape forced mesoscale circulations? *J. Geophys. Res.* **108**: 8854, DOI: 10.1029/2002JD003097.

Baldi M, Dalu GA, Pielke Sr RA. 2008. Vertical velocities and available potential energy generated by landscape variability – Theory. *J. Appl. Meteorol. Clim.* **47**: 397–410.

Blackadar AK. 1962. The vertical distribution of wind and turbulent exchange in a neutral atmosphere. *J. Geophys. Res.* **67**: 3095–3102.

Cheng WYY, Cotton WR. 2004. Sensitivity of cloud-resolving simulation of the genesis of a mesoscale convective system to horizontal heterogeneities in soil moisture initialization. *J. Hydrometeorol.* **5**: 934–958.

Childs PP, Qureshi AL, Raman S, Alapaty K, Ellis R, Boyles R, Niyogi D. 2006. Simulation of convective initiation during IHOP_2002 using the Flux-Adjusting Surface Data Assimilation System (FASDAS). *Mon. Weather Rev.* **134**: 134–148.

Clark TL. 1977. A small-scale dynamic model using a terrain-following coordinate transformation. *J. Comput. Phys.* **24**: 186–215.

Deardorff JW. 1974. Three-dimensional numerical study of the height and mean structure of a heated planetary boundary layer. *Boundary-Layer Meteorol* **7**: 81–106.

Deardorff JW. 1978. Efficient prediction of ground surface temperature and moisture, with inclusion of a layer of vegetation. *J. Geophys. Res.* **83**: 1889–1903.

Ek M, Mahrt L. 1991. A model for boundary-layer cloud cover. *Ann. Geophys.* **9**: 716–724.

Garcia-Carreras L, Parker DJ, Taylor CM, Reeves CE, Murphy JG. 2010. Impact of mesoscale vegetation heterogeneities on the dynamical and thermodynamic properties of the planetary boundary layer. *J. Geophys. Res.* **115**: D03102, DOI: 10.1029/2009JD012811.

Gopalakrishnan SG, Avissar R. 2000. An LES study of the impacts of land surface heterogeneity on dispersion in the convective boundary layer. *J. Atmos. Sci.* **57**: 352–371.

Gopalakrishnan SG, Baidya Roy S, Avissar R. 2000. An evaluation of the scale at which topographical features affect the convective boundary layer using large eddy simulations. *J. Atmos. Sci.* **57**: 334–351.

Górska M, de Arellano JV-G, LeMone MA, van Heerwaarden CC. 2008. Mean and flux horizontal variability of virtual potential temperature, moisture, and carbon dioxide: Aircraft observations and LES study. *Mon. Weather Rev.* **136**: 4435–4451.

Hopwood WP. 1995. Surface transfer of heat and momentum over an inhomogeneous vegetated land surface. *Q. J. R. Meteorol. Soc.* **121**: 1549–1574.

Huntingford C, Blyth EM, Wood N, Hewer FE, Grant A. 1998. The effect of orography on evaporation. *Boundary-Layer Meteorol* **86**: 487–504.

Jacquemin B, Noilhan J. 1990. Sensitivity study and validation of a land surface parameterization using the HAPEX-MOBILHY data set. *Boundary-Layer Meteorol* **52**: 93–134.

Kang S-L, Davis KJ. 2009. Reply. *J. Atmos. Sci.* **66**: 3229–3232.

Kang S-L, Davis KJ, LeMone M. 2007. Observations of the ABL structures over a heterogeneous land surface during IHOP_2002. *J. Hydrometeorol.* **8**: 221–244.

Kim H-J, Noh Y, Raasch S. 2004. Interaction between wind and temperature fields in the planetary boundary layer for a spatially heterogeneous surface heat flux. *Boundary-Layer Meteorol.* **111**: 225–246.

Kustas WP, Albertson JD. 2003. Effects of surface temperature contrast on land–atmosphere exchange: A case study from Monsoon 90. *Water Resour. Res.* **39**: 1159–1174.

LeMone MA, Grossman RL, McMillen RT, Liou K-N, Ou SC, McKeen S, Angevine W, Ikeda K, Chen F. 2002. CASES-97: Late-morning warming and moistening of the convective boundary layer over the Walnut River watershed. *Boundary-Layer Meteorol.* **104**: 1–52.

Lenschow DH, Sun J. 2007. The spectral composition of fluxes and variances over land and sea out to the mesoscale. *Boundary-Layer Meteorol* **125**: 63–84.

Letzel MO, Raasch S. 2003. Large eddy simulation of thermally induced oscillations in the convective boundary layer. *J. Atmos. Sci.* **60**: 2328–2341.

Mahrt L. 2000. Surface heterogeneity and vertical structure of the boundary layer. *Boundary-Layer Meteorol.* **96**: 33–62.

Mahrt L, Sun J, Vickers D, Macpherson JI, Pederson JR, Desjardins RL. 1994. Observations of fluxes and inland breezes over a heterogeneous surface. *J. Atmos. Sci.* **51**: 2484–2499.

Marsham JH, Parker DJ, Grams CM, Johnson BT, Grey WMF, Ross AN. 2008. Observations of mesoscale and boundary-layer scale circulations affecting dust transport and uplift over the Sahara. *Atmos. Chem. Phys.* **8**: 6979–6993.

Mason PJ. 1987. Diurnal variations in flow over a succession of ridges and valleys. *Q. J. R. Meteorol. Soc.* **113**: 1117–1140.

Mason PJ, Sykes RI. 1982. A two-dimensional numerical study of horizontal roll vortices in an inversion capped planetary boundary layer. *Q. J. R. Meteorol. Soc.* **108**: 801–823.

Morcrette C, Lean H, Browning KA, Nicol J, Roberts N, Clark P, Russell A, Blyth A. 2007. Combination of mesoscale and synoptic mechanisms for triggering an isolated thunderstorm: Observational case study of CSIP IOP 1. *Mon. Weather Rev.* **135**: 3728–3749.

Patton EG, Sullivan PP, Moeng C-H. 2005. The influence of idealized heterogeneity on wet and dry planetary boundary layers coupled to the land surface. *J. Atmos. Sci.* **62**: 2078–2097.

Prabha TV, Karipot A, Binford MW. 2007. Characteristics of secondary circulations over an inhomogeneous surface simulated with large-eddy simulation. *Boundary-Layer Meteorol.* **123**: 239–261.

Raasch S, Harbusch G. 2001. An analysis of secondary circulations and their effects caused by small-scale surface inhomogeneities using large-eddy simulation. *Boundary-Layer Meteorol.* **101**: 31–59.

Segal M, Arritt RW. 1992. Nonclassical mesoscale circulations caused by surface sensible heat-flux gradients. *Bull. Am. Meteorol. Soc.* **73**: 1593–1604.

Shao Y, Sogalla M, Kerschgens M, Brücher W. 2001. Effects of land-surface heterogeneity upon surface fluxes and turbulent conditions. *Meteorol. Atmos. Phys.* **78**: 157–181.

Shen S, Leclerc MY. 1995. How large must surface inhomogeneities be before they influence the convective boundary layer structure? A case study. *Q. J. R. Meteorol. Soc.* **121**: 1209–1228.

Taylor CM, Ellis RJ, Parker DJ, Burton RR, Thorncroft CD. 2003. Linking boundary-layer variability with convection: A case-study from JET2000. *Q. J. R. Meteorol. Soc.* **129**: 2233–2253.

Taylor CM, Parker DJ, Harris PP. 2007. An observational case study of mesoscale atmospheric circulations induced by soil moisture. *Geophys. Res. Lett.* **34**: L15801, DOI: 10.1029/2007GL030572.

Tian W-S. 2002. '*Orographic effects on convection*.' PhD thesis, pp 28–30. University of Leeds.

Tian W-S, Parker DJ. 2002. Two-dimensional simulation of orographic effects on mesoscale boundary-layer convection. *Q. J. R. Meteorol. Soc.* **128**: 1929–1952.

Tian W-S, Parker DJ. 2003. A modeling study and scaling analysis of orographic effects on boundary layer shallow convection. *J. Atmos. Sci.* **60**: 1981–1991.

Tian W-S, Parker DJ, Kilburn CAD. 2003. Observations and numerical simulation of atmospheric cellular convection over mesoscale topography. *Mon. Weather Rev.* **131**: 222–235.

Vosper SB, Brown AR. 2008. Numerical simulations of sheltering in valleys: The formation of nighttime cold-air pools. *Boundary-Layer Meteorol.* **127**: 429–448.

Walko RL, Cotton WR, Pielke RA. 1992. Large-eddy simulations of the effects of hilly terrain on the convective boundary layer. *Boundary-Layer Meteorol.* **58**: 133–150.

Weaver CP. 2004. Coupling between large-scale atmospheric processes and mesoscale land–atmosphere interactions in the U.S. Southern Great Plains during summer. Part I: Case studies. *J. Hydrometeorol.* **5**: 1223–1246.
Weaver CP, Avissar R. 2001. Atmospheric disturbances caused by human modification of the landscape. *Bull. Am. Meteorol. Soc.* **82**: 269–281.
Weckwerth TM. 2000. The effect of small-scale moisture variability on thunderstorm initiation. *Mon. Weather Rev.* **128**: 4017–4030.
Wieringa J. 1986. Roughness-dependent geographical interpolation of surface wind speed averages. *Q. J. R. Meteorol. Soc.* **112**: 867–889.
Wood N, Mason PJ. 1991. The influence of static stability on the effective roughness lengths for momentum and heat transfer. *Q. J. R. Meteorol. Soc.* **117**: 1025–1056.
Yates DN, Chen F, LeMone MA, Qualls R, Oncley SP, Grossman RL, Brandes EA. 2001. A Cooperative Atmosphere–Surface Exchange Study (CASES) dataset for analyzing and parameterizing the effects of land surface heterogeneity on area-averaged surface heat fluxes. *J. Appl. Meteorol.* **40**: 921–937.
Yi C, Davis KJ, Bakwin PS, Berger BW, Marr LC. 2000. Influence of advection on measurements of the net ecosystem–atmosphere exchange of CO_2 from a very tall tower. *J. Geophys. Res.* **105**: 9991–9999.